Corrosion Science 220 (2023) 111262

Contents lists available at ScienceDirect

Corrosion Science

journal homepage: www.elsevier.com/locate/corsci

Temperature dependence of high-temperature corrosion on nickel-based alloy in molten carbonates for concentrated solar power applications

Mickaël Lambrecht *, Gustavo García-Martín, María Teresa de Miguel, María Isabel Lasanta, Francisco Javier Pérez

Surface Engineering and Nanostructured Materials Research Group, Complutense University of Madrid, Complutense Avenue s/n, Madrid, Spain

ARTICLE INFO

Keywords:
Molten carbonates
Corrosion
High temperature materials

ABSTRACT

Concentrated solar power plants present several issues due to salt-induced corrosion, and the modelling of these mechanisms is needed for estimating power plants lifetime predictions. Moreover, a small variation of temperature can lead to microstructure changes due to allotropic transformations and thus free energy of formation of phases within the materials. Therefore, a corrosion study of molten carbonates, being high potential heat transfer fluids for CSP applications, on H230 alloy was performed at 700ºC, 750ºC and 800ºC up to 1000 h, in air atmosphere. The diffusion processes inducing the corrosion mechanism were analyzed and modelled with microstructural characterizations and thermogravimetric studies.

1. Introduction

Concentrated solar power plants combined with thermal energy storage are constantly evolving with the development of new heat transfer fluids. Molten carbonates are efficient over a wide range of temperatures and can operate in air atmosphere, offering high efficiency, as already studied in previous works mostly conducted on the behavior of this salt for fuel cells, thermal storage, and phase change material applications [1–11]. Tomczyk et al. investigated NiO and CoO electrodes in lithium-sodium carbonate (53–47 mol%) melt at 650ºC up to 120 h and concluded that lithium ion diffuse and incorporate nickel and cobalt oxide matrixes [12]. Sung-Goon et al. studied NiAl with the addition of lanthanum in lithium potassium carbonate (62–38 mol%) at 650ºC up to 100 h and showed that small quantities of this element increase the adherence of the oxide layer at cycling conditions. Cabeza et al. studied the corrosion behavior of AISI 304, OCT and IN702 alloys under lithium-potassium-sodium carbonates (30–57–13 mol%) at 550ºC up to 1000 h and found that Ni-based IN702 alloy showed the best performance, with the formation of Al_2O_3 and $NiCr_2O_4$ protective scales [13]. Moreover, they compared two alumina-forming alloys, respectively OC4 and HR224 in lithium-potassium sodium carbonates (32.1–34.5–33.4 wt%) at 650ºC up to 1000 h and found that HR224, whose composition in nickel is higher (45.53 wt%) than OC4 (26.16 wt %), showed a better corrosion resistance with a three-layered corrosion scale of NiO, $NiFe_2O_4$ and $CrFe_2O_4$ but potential spallation could occur for larger exposures [14]. This same mixture was tested by Xinhai et al., Hastelloy C276, Inconel 625 and Inconel 718 up to 500 h under argon atmosphere and IN617 showed the best potential with a mass gain inferior to 10 μm per year, and the formation of $FeNi_3$ and $LiCrO_2$/-$Li_2O{\cdot}Cr_2O_3$ [15]. Then, Nai-Qiang et al. studied a Fe-Cr-Al alloy in potassium-sodium carbonates (48–52 wt%) at 800ºC up to 720 h in static cycling conditions. They found that under an alumina layer, oxygen anion can diffuse along grain boundaries to finally form a dendritic oxide distribution, with a corrosion thickness between 2 and 8 μm under static conditions, and that significant change in surface morphology leads to harsh corrosion in cyclic ones [16,17].

Nickel-based alloys with high content of chromium seem to provide a good corrosion resistance against molten carbonates, with a tendency to form protective nickel-based spinel [18,19], but molybdenum compounds formed in the 5Fe-23Cr-58Ni-8Mo were solubilized in the eutectic during the immersion. Therefore, our work focused on the corrosion study of the nickel-based H230 alloy immersed in Li_2CO_3--Na_2CO_3-K_2CO_3 (32–33–35 wt%) at three different temperatures, respectively 700ºC, 750ºC and 800ºC, under air atmosphere. This material offers a high content in nickel and chromium with a low content of molybdenum (2 wt%.). Thermodynamical simulations coupled with microstructural characterizations will be performed to understand the corrosion mechanisms that can occur in a CSP plant with a high temperature window of a hundred degrees, to build models of predictions implementable in digital twins and to estimate the evolution of the

* Corresponding author.
E-mail address: milambre@ucm.es (M. Lambrecht).

https://doi.org/10.1016/j.corsci.2023.111262
Received 17 January 2023; Received in revised form 20 April 2023; Accepted 10 May 2023
Available online 12 May 2023

Table 1
Chemical composition of H230 (weight per cent).

Elements	Ni	Cr	W	Mo	Fe	Co	Mn	Si	Nb	Al	Ti	C	La	B
wt%	Bal.	22	14	2	3 max.	5 max.	0.5	0.4	0.5 max.	0.3	0.1 max.	0.1	0.02	0.015 max.

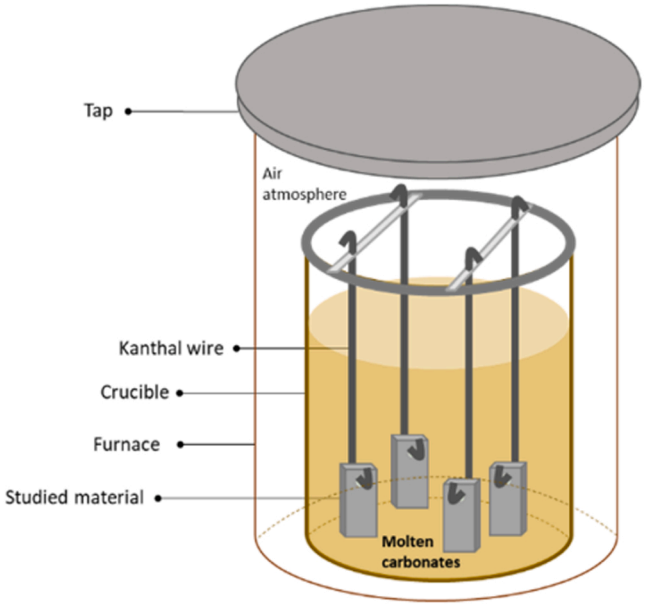

Fig. 1. Schematic representation of the corrosion test setup.

materials under real conditions.

2. Numerical and experimental methods

2.1. Thermodynamic simulations

CALPHAD (CALculation of PHAse Diagrams) methodology was used to perform thermodynamic calculations, with the help of Thermocalc Software. The stable phases forming in the defined system are calculated through the minimization of Gibbs energy of formation.

2.2. Corrosion testing

H230 samples, which composition can be found in Table 1, of 20 mm·10 mm·3 mm were grounded with abrasive sandpaper and cleaned with distilled water, then with ethanol, and dried. They were immersed in molten carbonates Li_2CO_3-Na_2CO_3-K_2CO_3 (32–33–35 wt%) at 700ºC, 750ºC and 800ºC, up to 1000 h, in a muffle furnace under air atmosphere, as seen in Fig. 1. The salt mixture consisted of Li_2CO_3 from VRW Chemicals with 99 % purity, Na2CO3 from Quimipur with 98.5 % purity and K2CO3 from Quimipur with 99 % purity and was held in 99,6 % pure alumina crucible of 200 cm^3.

During the corrosion test, samples were analyzed via gravimetric study at 0, 24, 72, 168, 250, 500, 750, and 1000 h. Kanthal wires were used to hold the samples and the system was optimized to avoid any

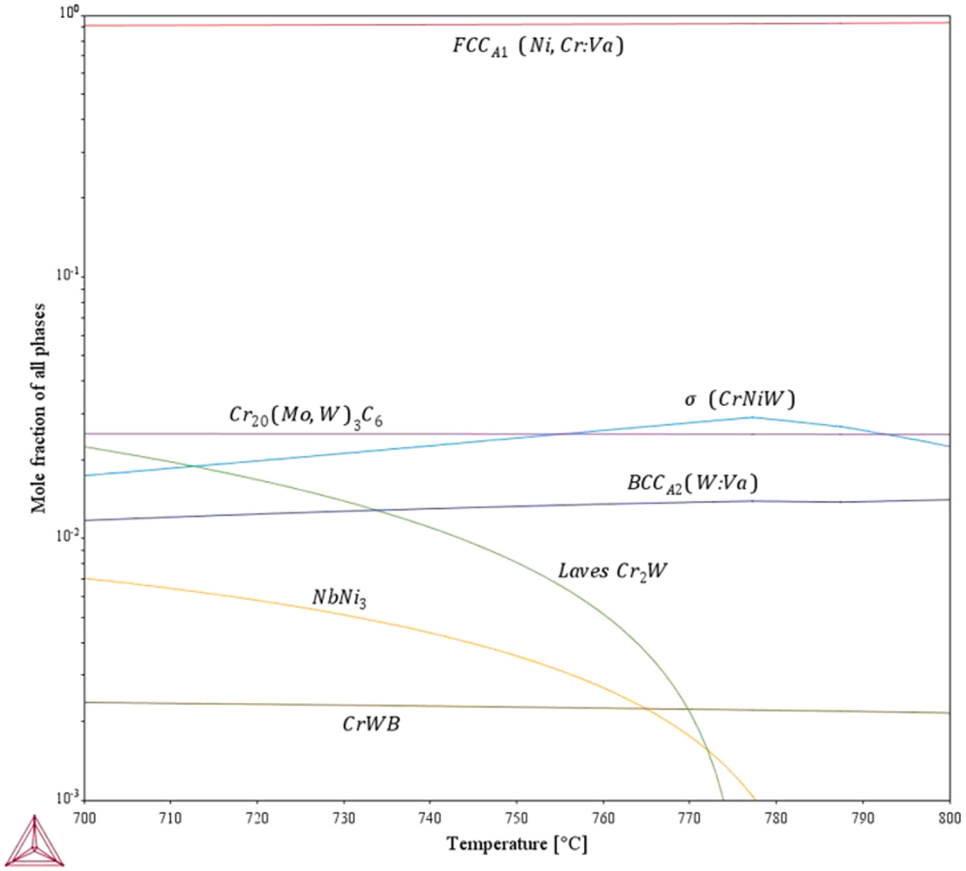

Fig. 2. Numerical simulation of the molar fraction of phases of H230 between 700ºC and 800ºC.

Table 2
OCP-IES analysis of the salt for each temperature at 500 h and 1000 h.

Time	0 h	500 h			1000 h		
Element (ppm)	Initial salt	700ºC	750ºC	800ºC	700ºC	750ºC	800ºC
Cl^-	282 ± 42	262 ± 39	277 ± 42	202 ± 30	221 ± 33	215 ± 32	127 ± 19
Ni	<1	73–74	4.7–5	6.0–6.3	20–21	<1	3–5
Cr	17.5–18	65–68	107–108	339–340	257–259	333–337	897–900
W	1.2–1.7	118–122	151–152	143–144	279–279.5	285–286	301–302
Mo	<1	8.0–8.8	10.0–10.1	12.8–12.9	19.8–20	20–20.6	30–32.5
Fe	6.8–8.5	11.5–13.4	3.3–6.0	9.5–14	17–20	20–29	40–68
Co	<1	1.19–1.25	<1	<1	<1	<1	2.55–2.64
Mn	<1	1.90–1.92	1.6–1.9	3.9–4.2	4.7–4.8	6.7–6.9	16.2–16.4
Si	30–30.4	14.9–16.9	15.5–15.7	15.7–16.1	48–50	37–41	32–34
Nb	<1	<1	<1	<1	<1	<1	<1
Al	39–46	162–164	30–31	32–38	104–110	17.4–17.5	19.2–21
Ti	1.88–1.95	2–3.4	1.7–1.8	1.6–1.9	1.35–1.4	<1	<1
Mg	24–28	11.8–11.9	1.1–1.6	1.5–1.7	11.5–11.7	8.5–9.6	1.7–2.5
S	96–102	94–100	114–115	87–102	100–114	100–109	113–123

influence on the test. At each time, a sample were removed, cooled, and rinsed with boiling water to remove the remaining salt. Four replicates were used to perform each test and the average of their weight variation was considered for the gravimetric results. The formula (Eq. 1) used to calculate the mass gain over time was as follows:

$$\frac{\Delta m}{S_0} = \frac{m_f - m_i}{S_0} \quad with \quad \left\{ \begin{array}{c} m_i \ \ the \ \ initial \ \ mass \\ m_f \ \ the \ \ mass \ \ at \ \ the \ \ selected \ \ time \\ S_0 \ \ the \ \ sample's \ \ initial \ \ area \end{array} \right\} \tag{1}$$

Scanning Electron Microscopy – Energy Dispersive Xray spectroscopy (SEM-EDX) analyzed the morphology and chemical composition of the corrosion layer, with a JEOL® JSM-820 scanning electron microscope, which operated at 25 kV and was equipped with a backscattered electron detector. EDX analyses were carried out with a recommended working distance of 10 mm. X-ray diffraction (XRD) was helped to identify the crystalline phases present on the samples surfaces, with a PANalytical® (X'Pert PRO MRD model) diffractometer and a copper target (Kα1 = 1.54056 Å y Kα2 = 1.54439 Å). Analyses were carried out at a voltage of 45 kV and 40 mA of current, from 20∘ and 90∘, a step size of 0.05∘ and 3 s of measuring time per step, and an angle of 0.5∘ for grazing incidence. Standard patterns used for crystalline compounds identification correspond to those compiled by Joint Committee on Powder Diffraction Standards (JCPDS) Committee. The elemental composition of the salts before and after the experiments were quantified by the means of inductive coupled plasma,-optical emission spectrometry (ICP-OES) for the metallic elements and the Volhard method for the chlorides.

3. Experimental results

3.1. Thermodynamic simulations

H230 alloys were simulated to calculate the mole fraction of stable phases forming between 700ºC and 800ºC, as seen in Fig. 2. Indeed, the major presence of nickel, chromium, and tungsten lead to the presence of the face-centered cubic Ni-Cr matrix with precipitation of σ-phase CrNiW increasing with temperature, reaching a maximum Gibbs energy of formation at 777ºC, and then decreasing, showing that its higher molar fraction will be at the experimental temperature of 750ºC. Moreover, $Co_{23}(Mo,W)_3C6$ carbide molar fraction precipitates and is stable over temperature. Plus, tungsten body-centered cubic is also predicted in the matrix, along with small quantities of CrWB. Finally, chromium-tungsten laves phase are stable at 700ºC but unstable over temperature, with a complete dissolution at 773ºC, as well as $NbNi_3$ dissolving at 778ºC.

3.2. Salt analysis

Table 2 gathers the salt analyses performed at 500 h and 1000 h to highlight the diffused elements during the corrosion mechanisms, compared to the initial composition. First, chlorine ion, present in

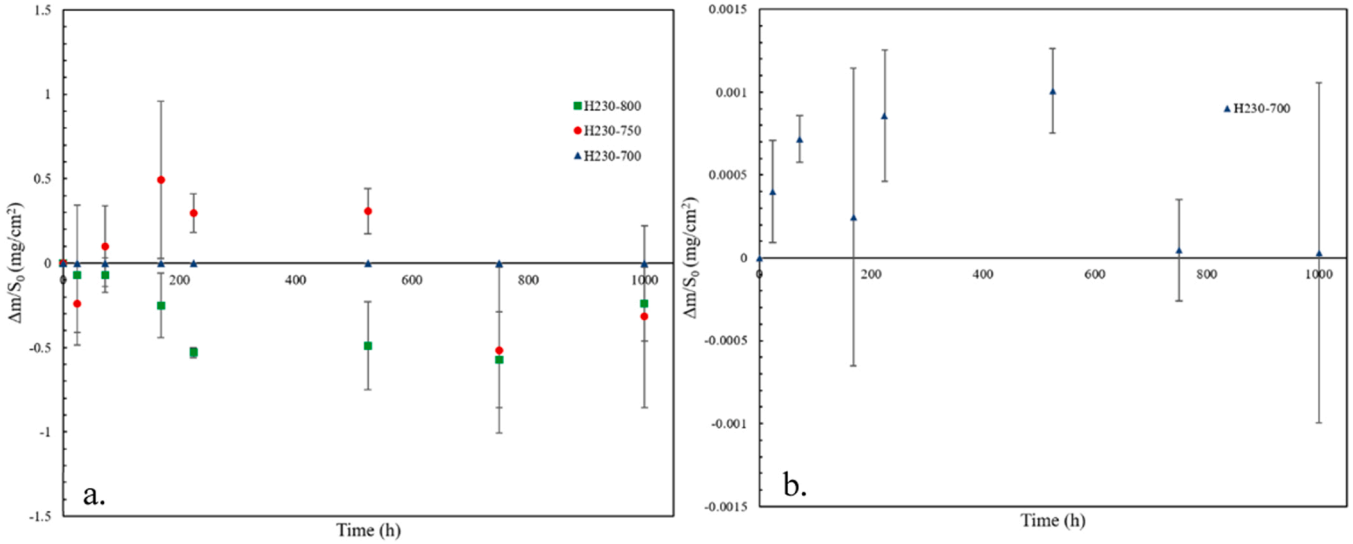

Fig. 3. Thermogravimetric analysis of H230 at a. 700ºC, 750ºC and 800ºC and b. a focus at 700ºC.

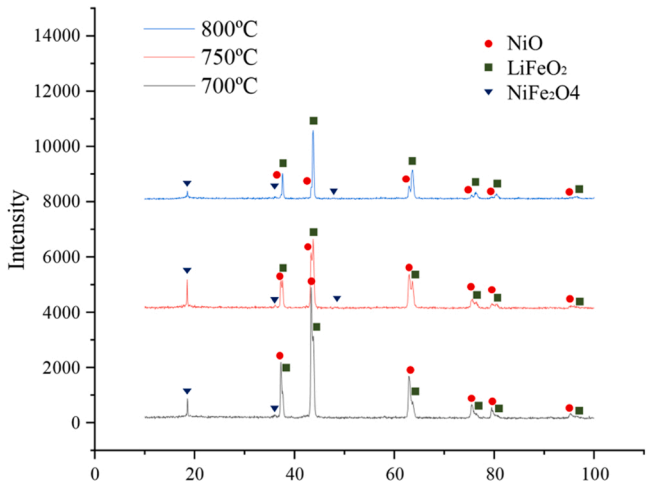

Fig. 4. XRD analysis of H230 samples after immersion at 700ºC, 750ºC and 800ºC.

highest quantity as impurity (282 ± 42 ppm) decreases over time, and the diffusion process is accelerated by the temperature. The same behavior can be observed with titanium and magnesium, in smaller quantities. Then, nickel, chromium, tungsten, iron, and aluminum seemed to actively participate in the outward diffusion process from the substrate to the salt. Indeed, the higher concentration variation occurred in chromium, 51 times the initial amount at 800ºC and 1000 h, and 3.2 times more than at 700ºC. Finally, the aluminum element was detected with an increase in amount only at 700ºC, whereas it slightly decreases at 750ºC and 800ºC.

3.3. Thermogravimetric analysis

Mass loss measurements led to the description of three different behaviors for each temperature, as seen in Fig. 3a. First, a uniform scale permits to observe the linearity and quasi-null mass variation of H230 at 700ºC. At 750ºC, an initial mass loss at 24 h followed by a gain plus a stabilization from 250 h to 500 h can be analyzed as the first spallation of an outer layer and then passivation. Then, the strong loss at 750 h could be interpreted as delamination of this oxide scale. In parallel, at 800ºC the alloy suffered from potential spallation but did not show a further gain, with a similar stabilization from 250 h to 750 h. Finally, both materials at 750ºC and 800ºC showed a similar mass gain up to 1000 h. Indeed, in Fig. 3b, a relative scale for the sample at 700ºC permits observing a mass variation identifiable as passivation, but a return to its initial mass at 750 h, that seems stable up to 1000 h. Thus, the mass losses were used at 524 h to estimate the corrosion rate following the ASTM G1 – 03(2017)e1 standard "Standard Practice for Preparing, Cleaning and Evaluating Corrosion Test Specimens", with Eq. (2) and resulted in, for 700ºC, 750ºC and 800ºC respectively, corrosion rates of 0.019 ± 0.005, 5.763 ± 2.502 and − 9.135 ± 4.847 µm/year. However, these values cannot be taken as reference as longer exposures need to be performed but can be compared.

$$CR\ \left(\frac{\mu m}{year}\right) = \frac{\Delta m}{S_0}\cdot\frac{8.76\cdot 10^7}{\rho\cdot t} \quad with \quad \left\{\begin{array}{llll} \rho & the & density & \left(g\cdot cm^3\right) \\ t & the & exposure & time \ (h) \end{array}\right\} \tag{2}$$

3.4. Superficial analysis

3.4.1. XRD analysis

X-ray diffraction permitted to identify and understand the crystalline evolution of H230 for each temperature, as seen in Fig. 4. Cubic NiO, $LiFeO_2$ and $NiFe_2O_4$ are present in all samples, but the expansion of $LiFeO_2$ can be highlighted, with its peak intensities taking over and compensating the diminution of NiO ones, along with $NiFe_2O_4$ peaks diminishing with temperature.

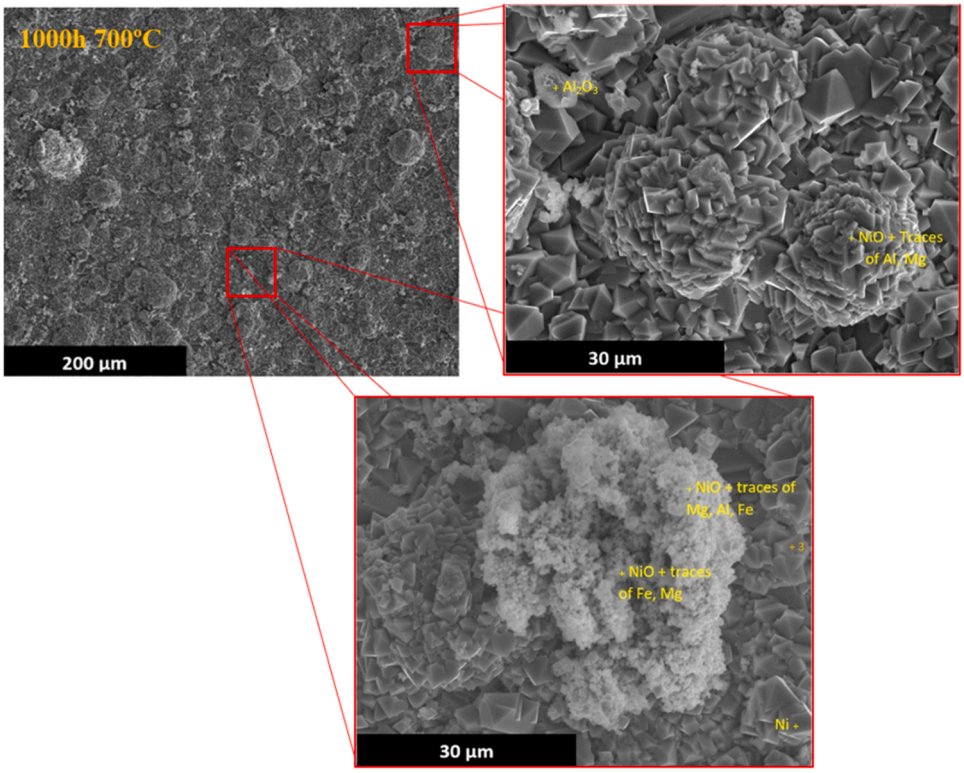

Fig. 5. SEM superficial analysis at 700ºC-500 h.

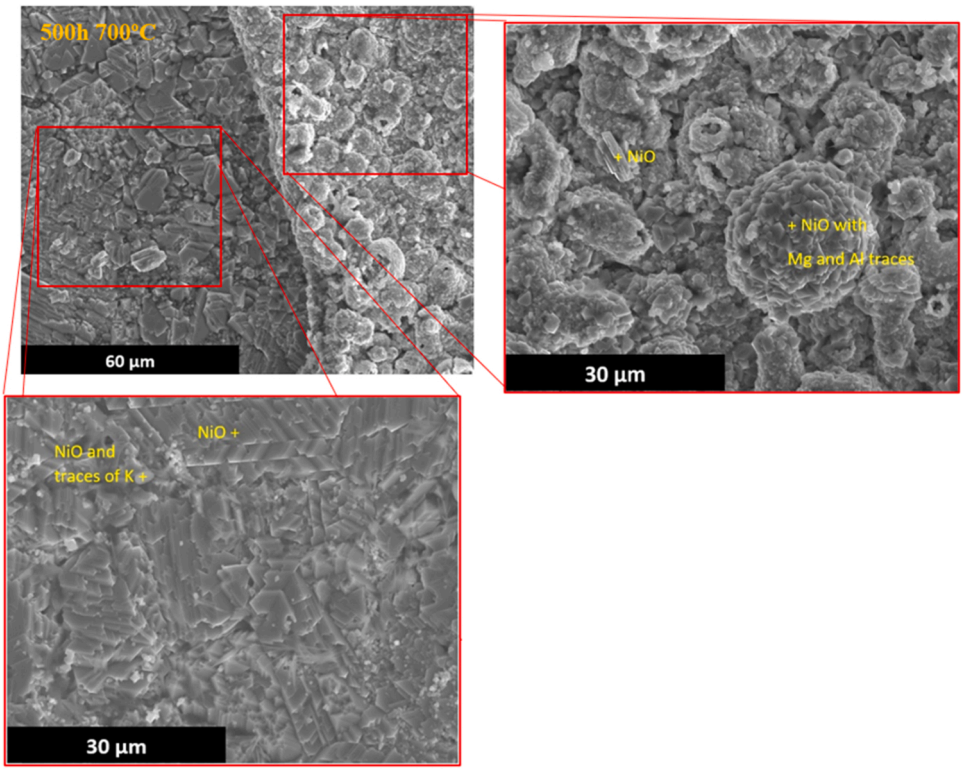

Fig. 6. SEM superficial analysis at 700°C-1000 h.

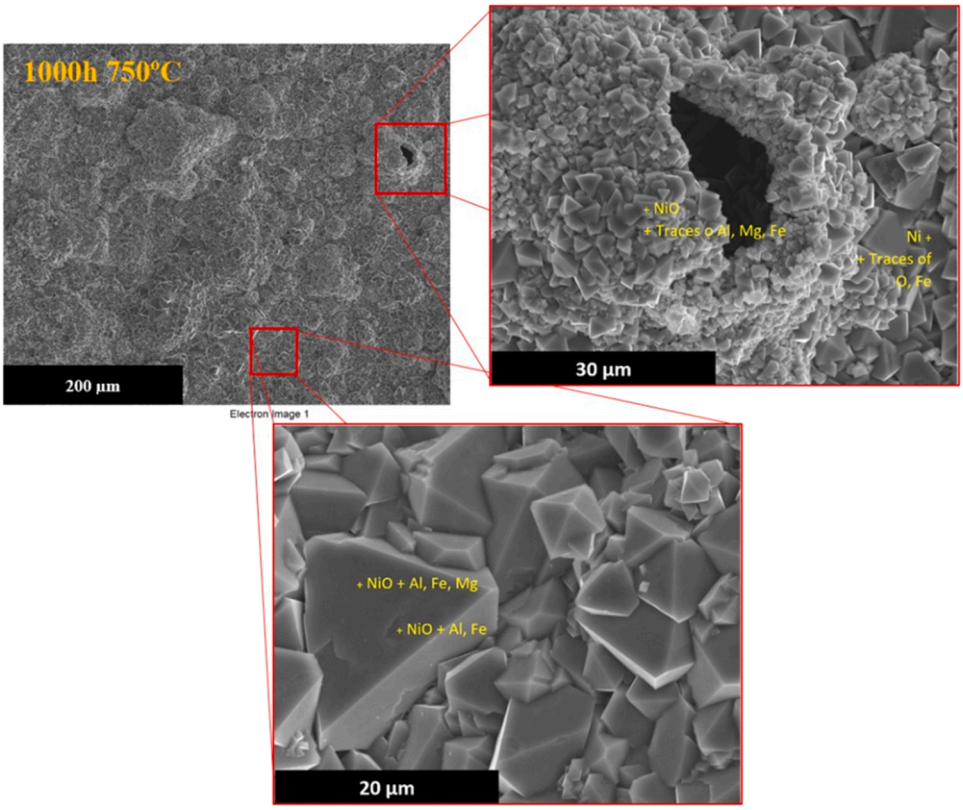

Fig. 7. SEM superficial analysis at 750°C-500 h.

3.5. SEM analysis

SEM-EDS superficial analyses were performed at 500 h and 1000 h, to understand the behavior of H230 with respect to time and temperature. Nevertheless, the lithium element cannot be detected with this technique.

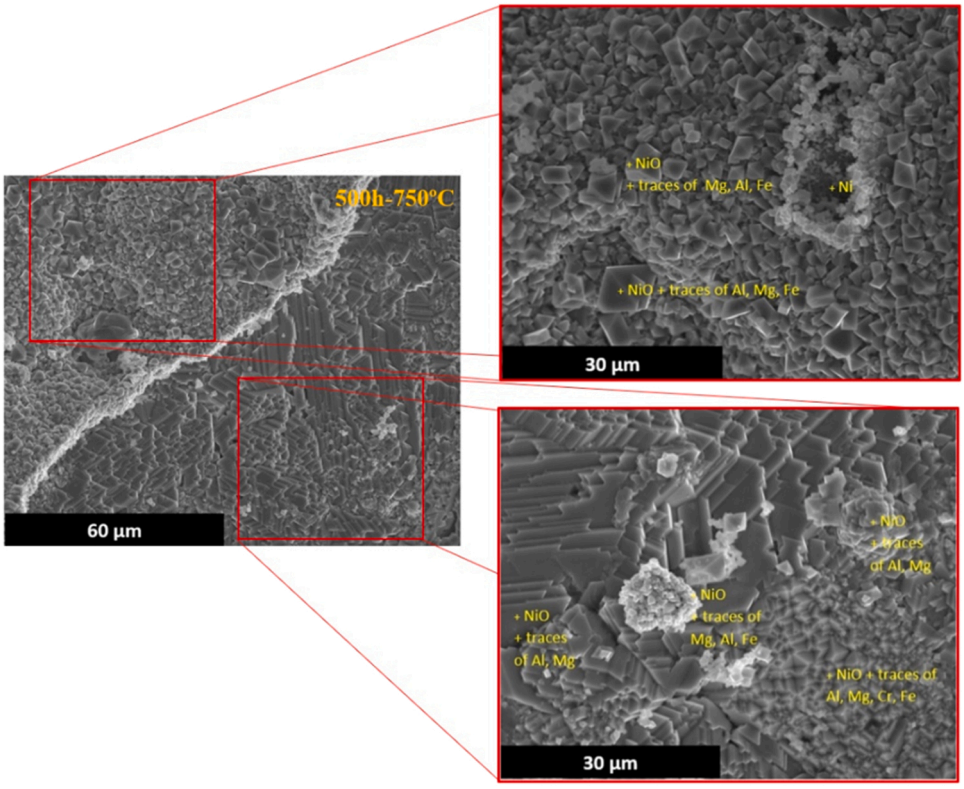

Fig. 8. SEM superficial analysis at 750ºC-1000 h.

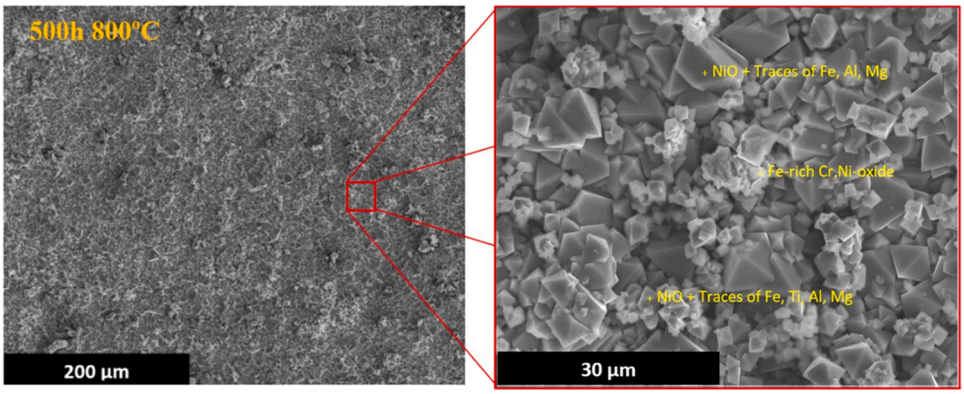

Fig. 9. SEM superficial analysis at 800ºC-500 h.

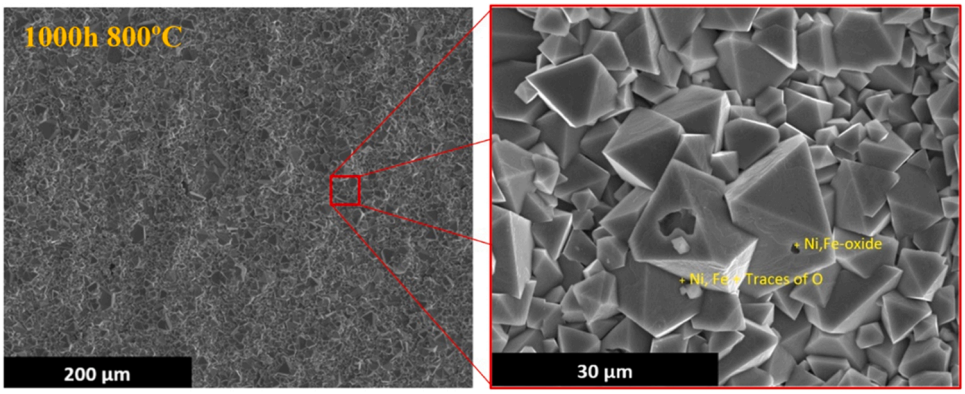

Fig. 10. SEM superficial analysis at 800ºC-1000 h.

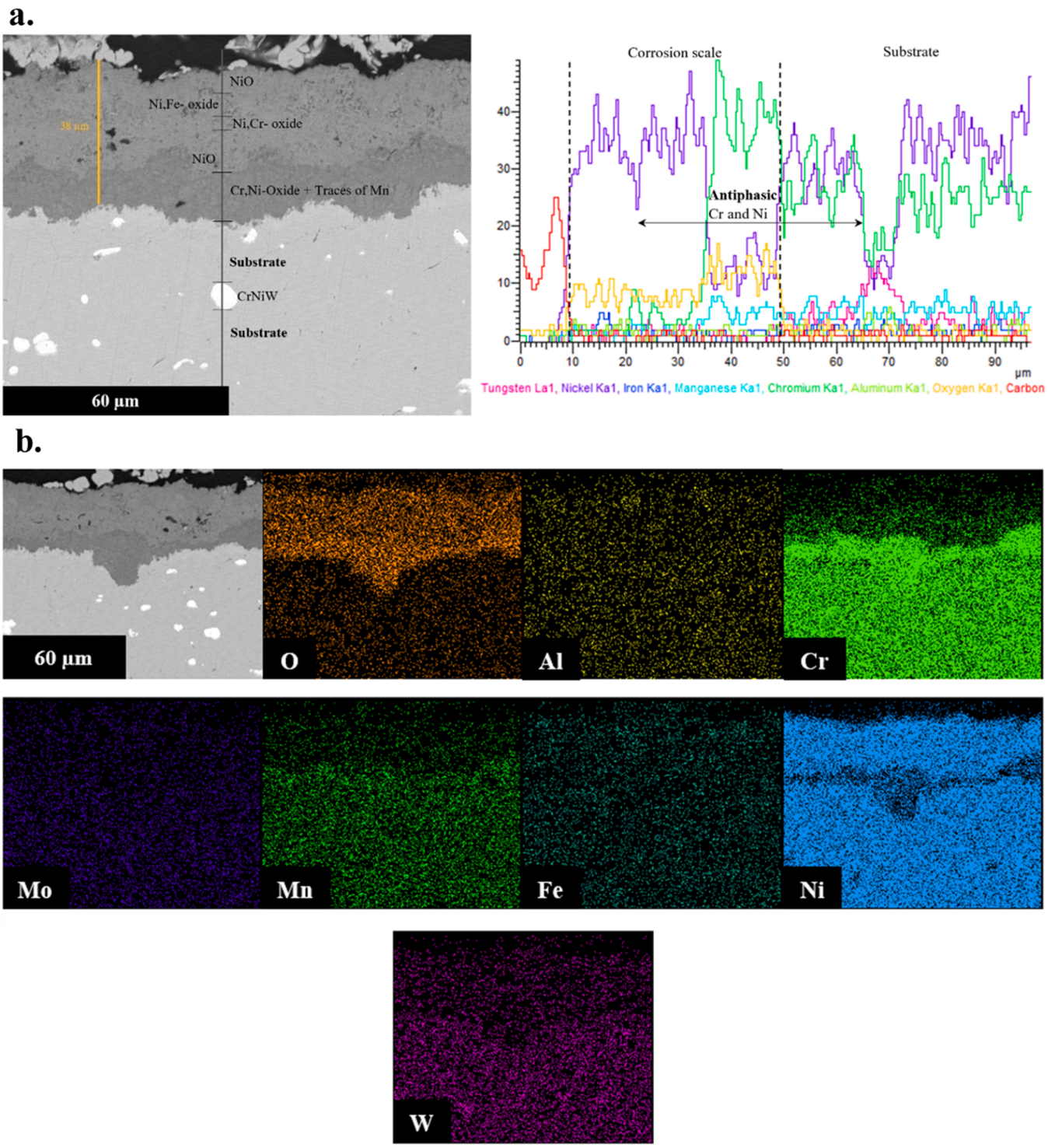

Fig. 11. SEM cross analysis at 700ºC-500 h with a. line scan and b. mapping.

At 700ºC and 500 h in Fig. 5, a bilayer can be observed, stemming from the spallation of a superficial oxide layer, relating to the later mass loss on gravimetric analysis. The inner one presents nickel oxide plates as a vicinal surface, with steps in the order of 1–2 µm. Then, the outermost layer presents the same compositions, but as spherical grains with traces of magnesium and aluminium. At 1000 h, in Fig. 6, the main surface of spherical oxide growth and traces of aluminium and magnesium are identifiable. Moreover, the alumina phase is also detected, stemming from the oxidation of outward diffused aluminium.

At 750ºC and 500 h in Fig. 7, a similar bilayer can be observed but with traces of magnesium, aluminium, and iron in both layers. Again, the inner layer shows vicinal plates of NiO whereas the external microstructure presents cubic crystals. Then at 1000 h in Fig. 8, a single hilly surface is identified as NiO, with traces of aluminium, magnesium, and iron on an apparent skin of the crystal. Nevertheless, a hole can be pointed out underlying the potential formation of a porous microstructure in the oxide scale. Indeed, constrained salt in the layer can lead to an outgazing of saturated vapor pressure pressurizing into the pore.

Interestingly, at 800ºC and 500 h in Fig. 9, a single oxide scale is present with traces of iron, titanium, aluminium, and magnesium,

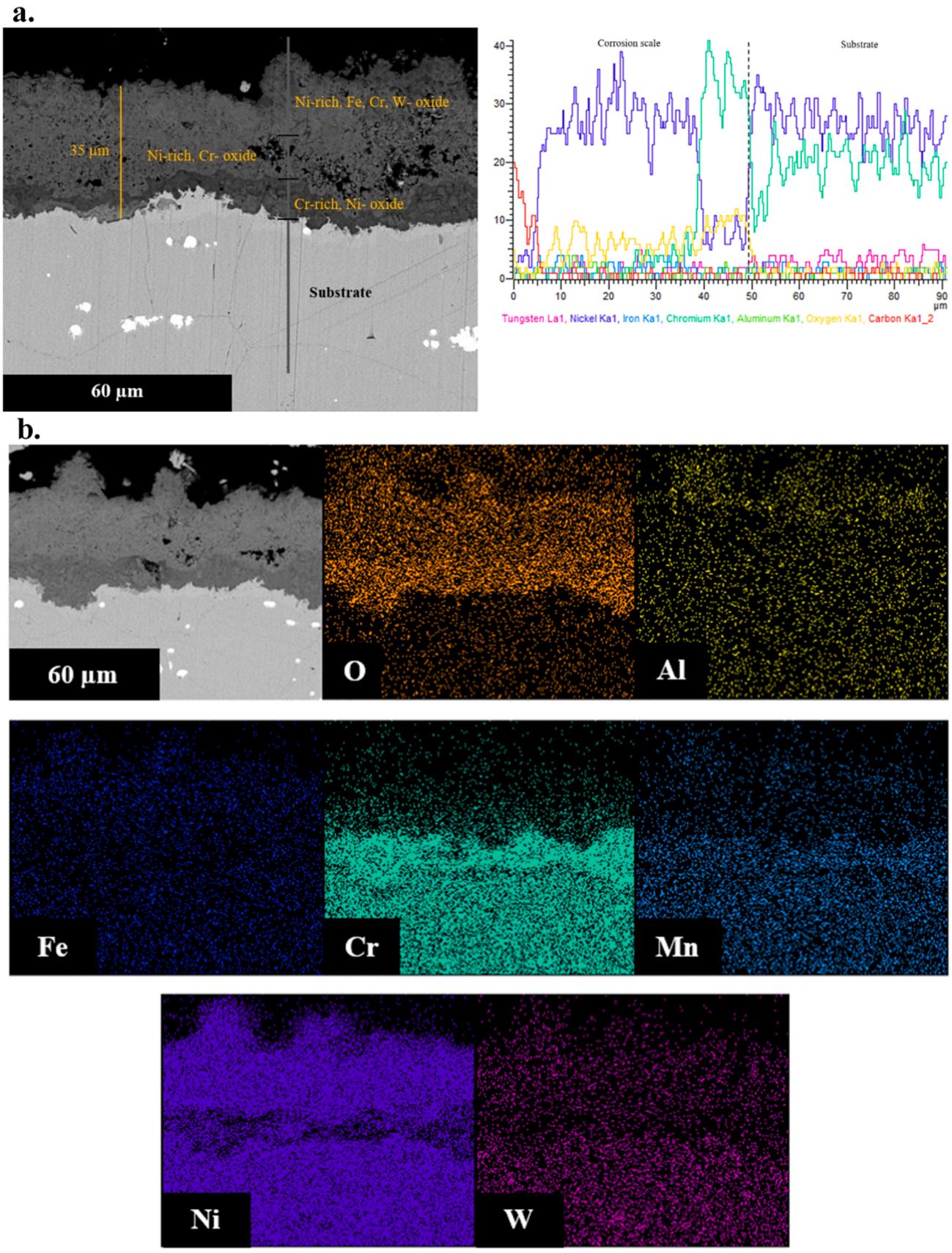

Fig. 12. SEM cross analysis at 700ºC-1000 h with a. line scan and b. mapping.

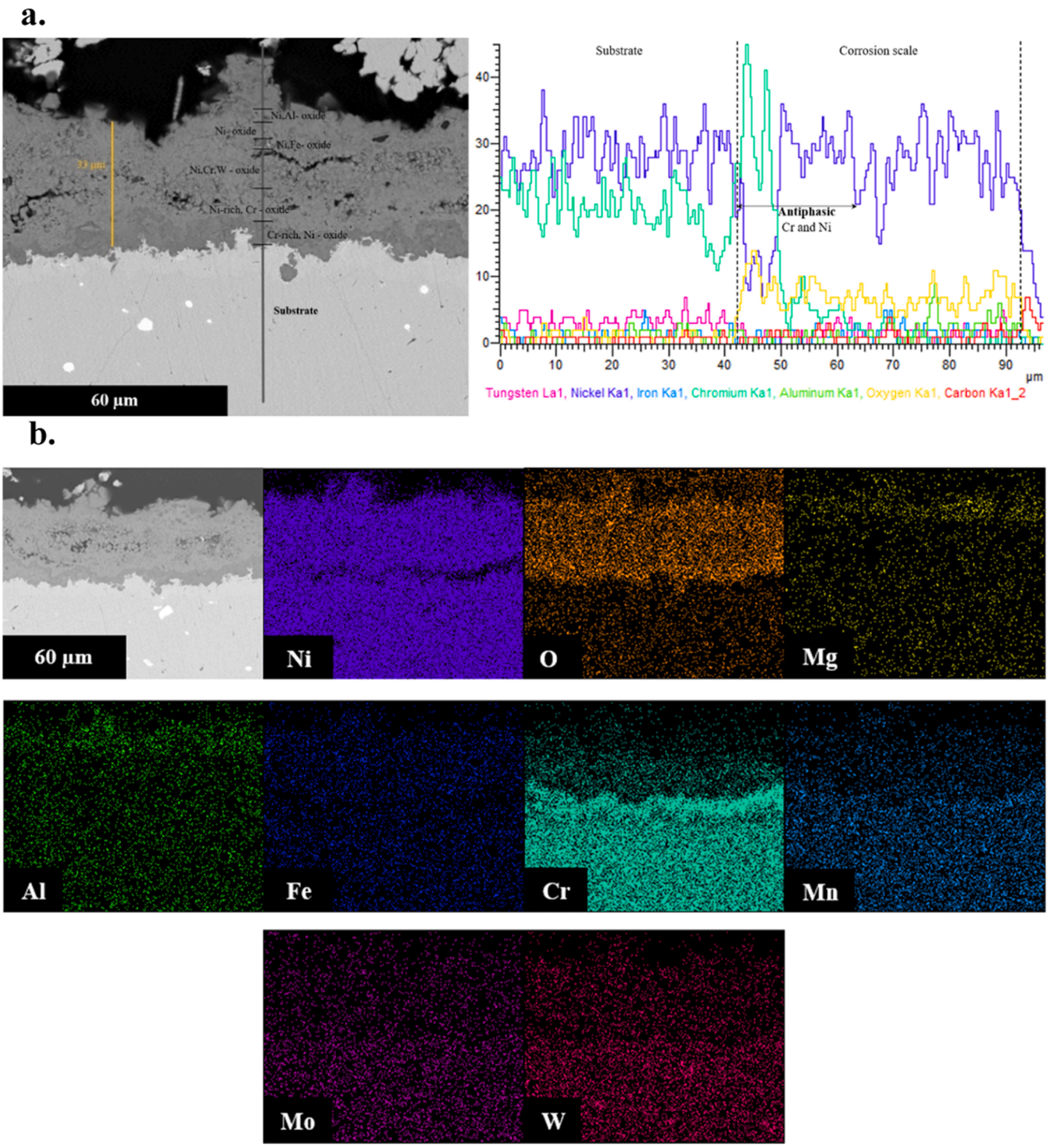

Fig. 13. SEM cross analysis at 750ºC-500 h with a. line scan and b. mapping.

surrounded by iron-rich chromium oxide, showing chromium outward diffusion. The chromium presence can witness the early stage of chromia formation and precursor of $LiCrO_2$ phase [15], but was cannot be identified as it was not detected by XRD patterns. Plus, at 800ºC and 1000 h in Fig. 10, nickel-iron oxide is identified, with the evidence of a spalled layer. Iron traces may also be linked with the presence of $LiFeO_2$ phase at the surface, as highlighted by XRD.

3.6. Cross analysis

Cross analyses were performed for each sample with SEM-EDS mapping. At 700ºC and 500 h in Fig. 11a, a 38 µm oxide bilayer is visible with an outermost one mainly composed of nickel oxide, and the inner one of chromium-rich, nickel oxide, with traces of manganese. The lineal spectra show an antiphase behavior of chromium and nickel all over the oxide scale resulting from chromium atoms taking the place of nickel in the oxide crystalline structure. A part of the iron-containing nickel oxide under the outermost layer can be also identified as

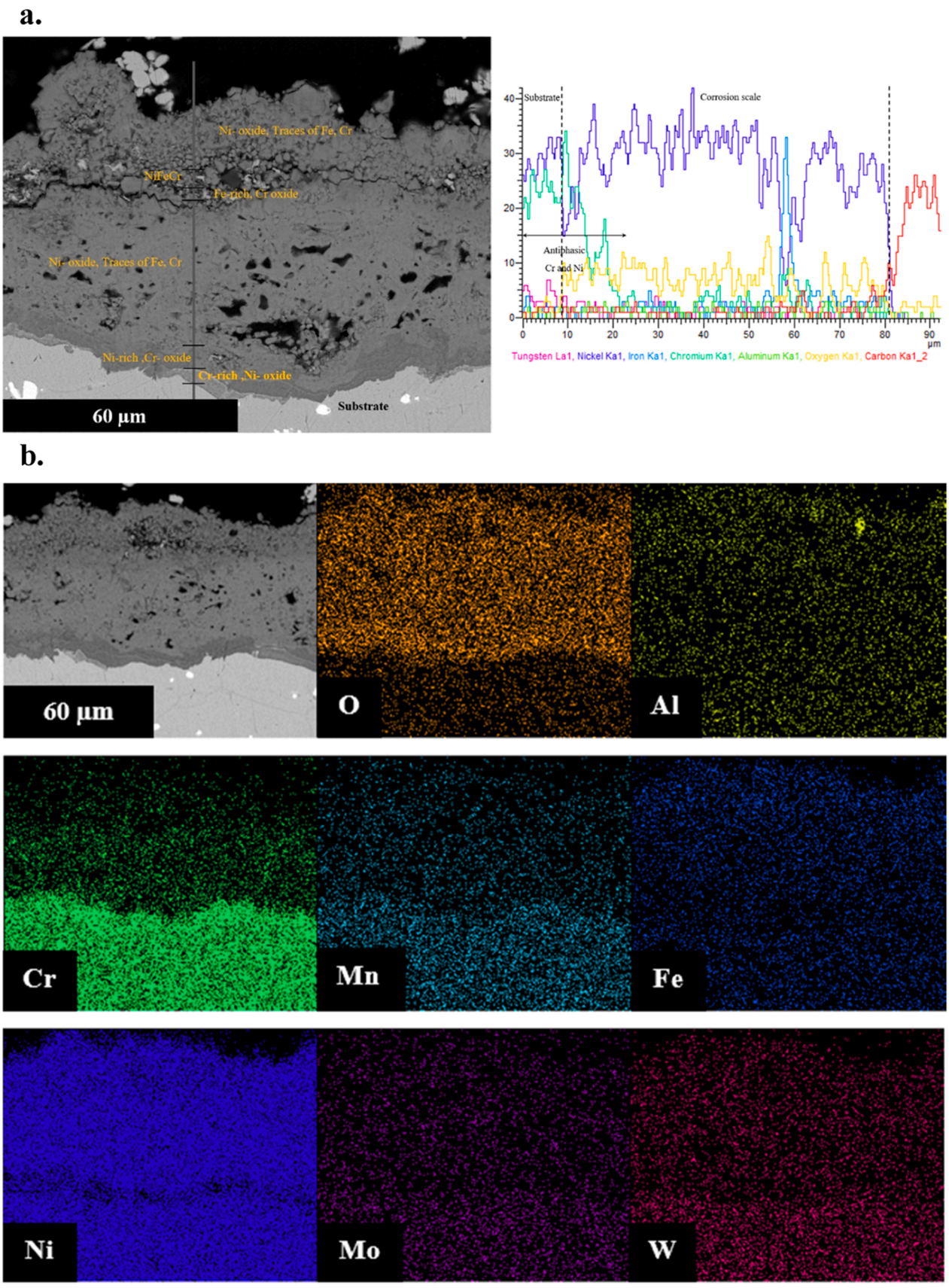

Fig. 14. SEM cross analysis at 750ºC-1000 h with a. line scan and b. mapping.

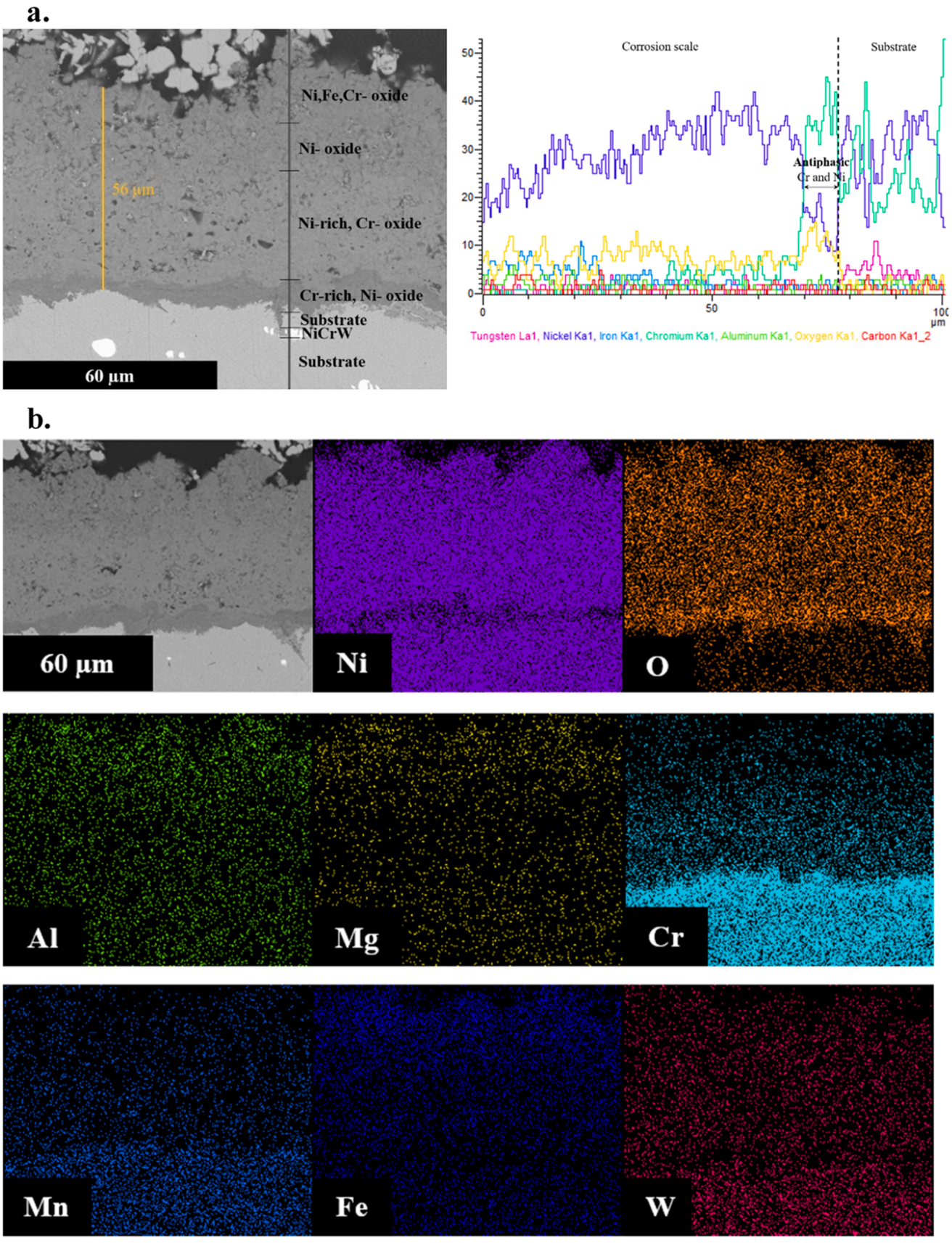

Fig. 15. SEM cross analysis at 800ºC-500 h with a. line scan and b. mapping.

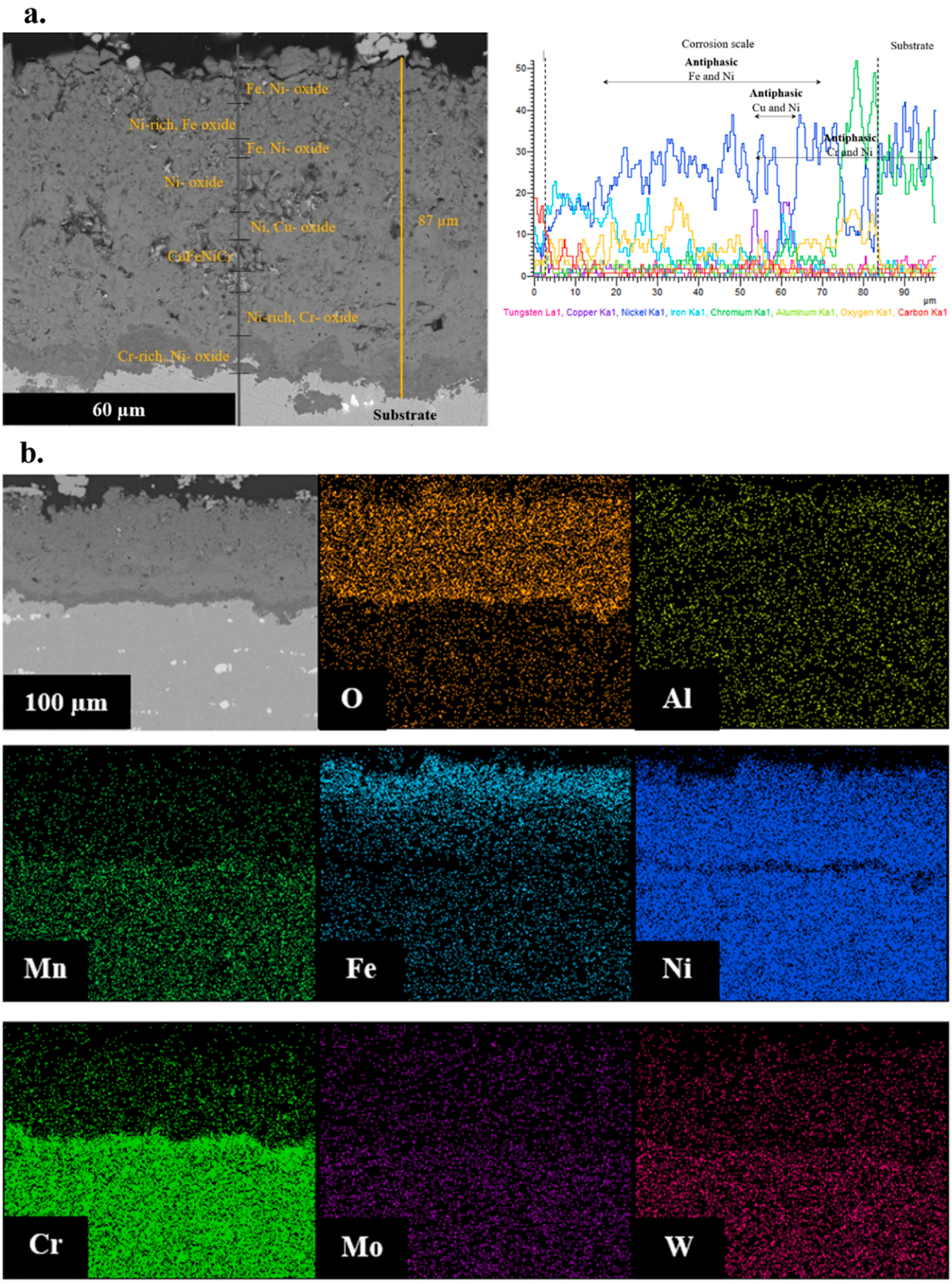

Fig. 16. SEM cross analysis at 800ºC-1000 h with a. line scan and b. mapping.

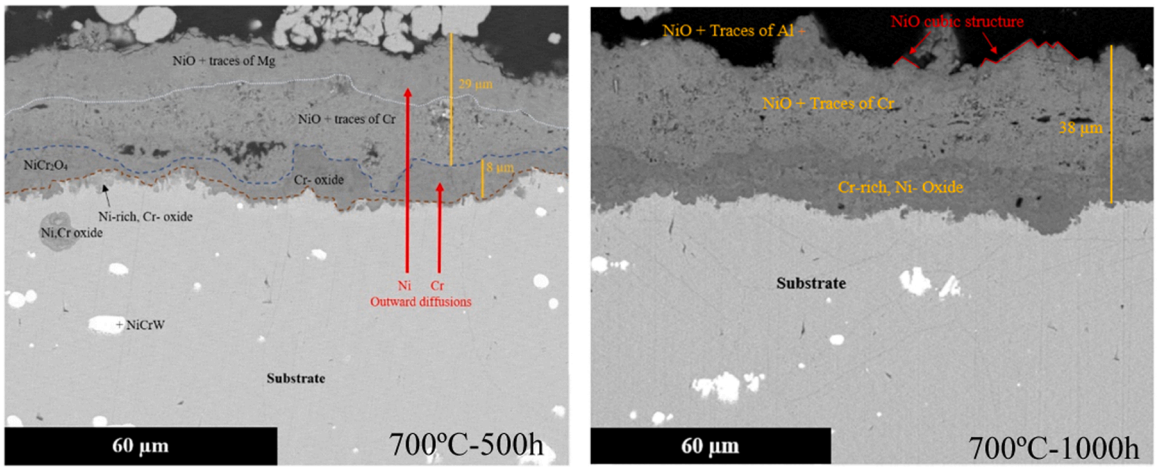

Fig. 17. SEM cross analysis at 700ºC for 500 h and 1000 h.

$LiFeO_2$. Indeed, EDS mapping in Fig. 11b permits us to visually see the lack of nickel in the Cr-rich oxide zone. Plus, tungsten also presents a slighter lack of presence in this zone, and manganese outward diffusion seems mitigated by this layer. Brighter zones of aluminium on the top of the corrosion scale and tungsten in the white grains of the substrate can also be observed.

Then, at 700ºC and 1000 h in Fig. 12a, a line scan has been performed in another part of the sample, presenting a 35 µm oxide scale. Traces of iron, chromium, and tungsten can be pointed on the outermost layer, forming the NiO-$LiFeO_2$ scale, above a porous nickel-rich chromium-oxide, where the diffused elements are not present. Indeed, their outward diffusion leads to the creation of voids. Plus, the inner layer is composed of chromium-rich, nickel oxide.

EDS mapping in Fig. 12b shows the evidence of an aluminum-iron-tungsten outward diffusion, as present in two grains formed at salt-alloy interfaces, within a nickel oxide matrix. In the meantime, the chromium-rich oxide can be observed in the inner layer, where nickel and tungsten show a lack of presence.

At 750ºC and 500 h in Fig. 13a, a 33 µm oxide scale can be observed but with pores and crack on the thicker outermost one. At this temperature, iron, aluminium, and tungsten have diffused enough to be considered in the corroded layer as components of oxide compounds, and iron-lithium oxide is further forming. Indeed, nickel oxide is the main detected one, but the presence of nickel-aluminium oxide and nickel-iron oxide can be estimated. Plus, the inner layer remains chromium-rich, with nickel oxide. EDS mapping in Fig. 13b emphasizes the presence of aluminum and magnesium on the top and relates the Cr-rich oxide action as a barrier to manganese diffusion and its repelling behavior of nickel, molybdenum, and tungsten.

At 750ºC and 1000 h in Fig. 14a, the line scan permits to analysis a multilayered oxide microstructure. On the outermost layer, traces of iron and chromium can be pointed out, with a granular morphology. The outer presence of iron can explain the increase of $LiFeO_2$ peak in XRD at this temperature. Plus, a lack of oxygen underneath shows nickel-iron-chromium precipitation, above an iron-rich chromium-oxide. Then, a denser nickel-oxide with traces of iron and chromium layer can be observed, although large voids are present. Moreover, those two main layers are separated by a crack. Finally, the inner layer can be divided into two sublayers, where chromium diffusion can be observed, presenting a nickel-rich chromium-oxide above a chromium-rich nickel-oxide. In parallel, EDS mapping in Fig. 14b shows a thin concentration of iron and aluminum on the top of the oxide layer, along with oxygen. Plus, this mapping permits to consider of the manganese coherence with chromium, in which outward diffusion is mitigated by the Cr-rich layer. Furthermore, this layer presents a slight lack in the concentration of nickel, molybdenum, and tungsten.

At 800ºC and 500 h in Fig. 15, a 56 µm oxide layer is observable, with a granular morphology composed of an outermost layer of nickel-iron-chromium oxide, nickel oxide and a denser nickel-chromium oxide. Then, a chromium-rich nickel oxide layer makes the bridge between the top layers and the substrate. Plus, this scale shows an antiphase line scan of nickel in a matrix of chromia, that could suppose the inclusion of

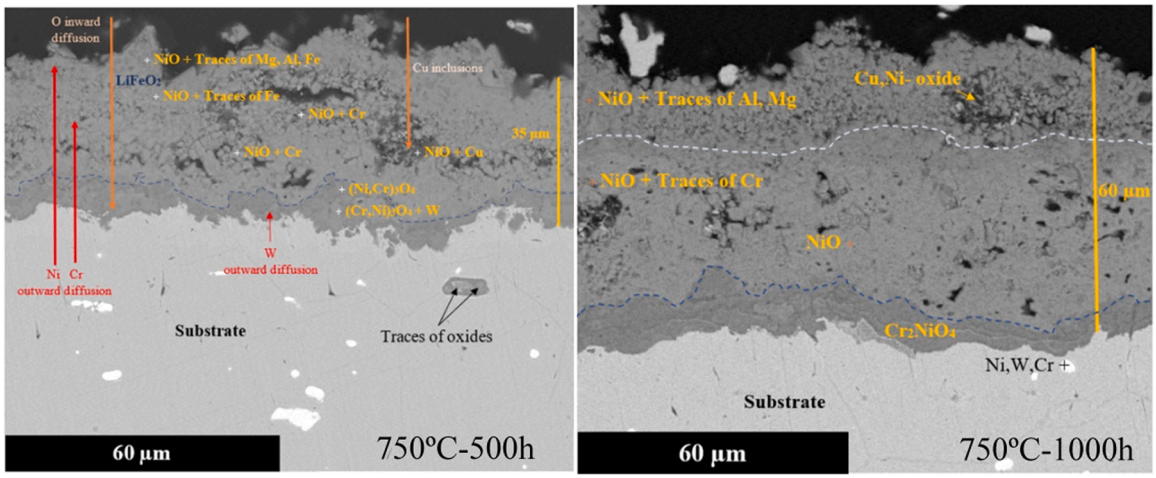

Fig. 18. SEM cross analysis at 750ºC for 500 h and 1000 h.

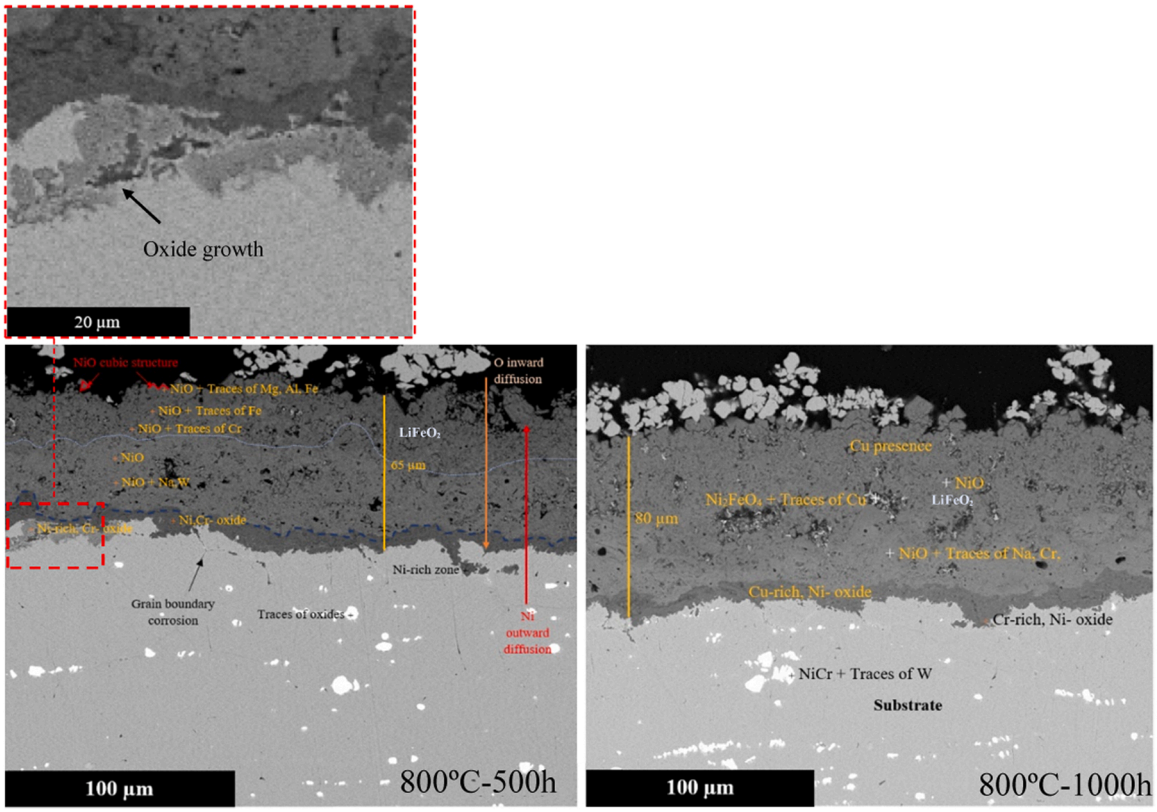

Fig. 19. SEM cross analysis at 800°C for 500 h and 1000 h.

nickel atoms into a previous chromia formation to potentially form a spinel. The latter layer interface with the substrate is not continuous and shows a thin dendritic dispersion of the oxide at grain boundaries.

In parallel, at 800°C and 1000 h on Fig. 16a, an 87 µm oxide scale can be observed. The outer layer consists of a granular iron-nickel oxide and Ni-rich iron-oxide, above a denser nickel oxide, nickel oxide, and iron-nickel oxide, all with copper inclusions. This copper concentration may come from the embedding process of the sample witnessed the large presence of voids in the corrosion layer. Plus, the line scan permits observing three layers of interdiffusion of iron, copper, and chromium,

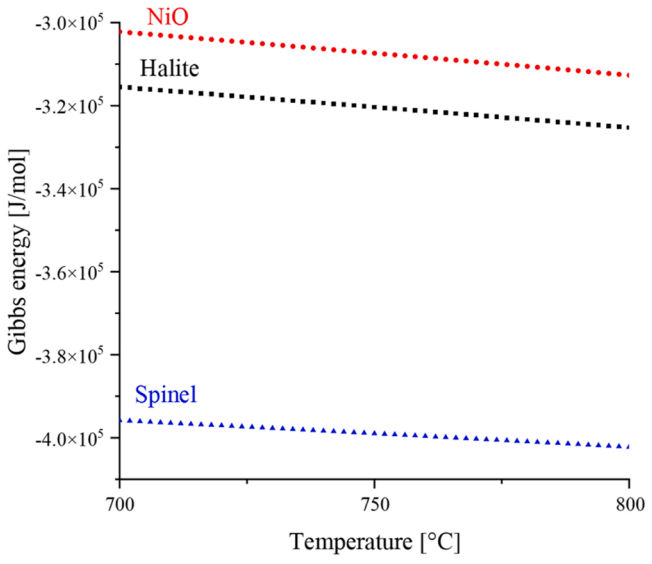

Fig. 20. Numerical simulation of the Gibbs energy of stable phases of a Mg,Al, Fe-NiO matrix system with temperature.

exchanging with nickel sites in the NiO matrix. Furthermore, this phenomenon occurs with copper in a medium range, where iron and chromium interdiffusion coexist. This result highlights the enhanced void formation between these two corrosion layers. Moreover, the discontinuous interface between the inner Cr-rich nickel oxide and the substrate is characterized by coarse oxides precipitated from grain boundaries. Moreover, molybdenum and tungsten outward diffusion can be visualized even though they are lacking at the inner chromium-rich oxide with traces of manganese, along with an absence of nickel and iron. Indeed, iron is the major component in the outermost layer showing its reactivity with lithium and nickel to form and $LiFeO_2$ a nickel-iron spinel layer respectively.

4. Discussion

4.1. On the oxide formation

Fig. 17, Fig. 18, and Fig. 19 depict the diffusion mechanism and proposed phases formation at 700°C, 750°C and 800°C respectively, with respect to their exposure time. At 700°C, it can be observed a stable oxide formation with a mean thickness going from 37 µm to 38 µm, composed of an outer layer of nickel oxide with remarkable triangular shapes at 1000 h, then chromium oxide and the inner layer identified as $NiCr_2O_4$. Besides nickel and chromium, aluminum participated in the outward diffusion mechanism. Then, at 750°C, the oxide layer showed a poor stability with a mean thickness going from 35 µm at 500 h to 60 µm at 1000 h. Indeed, nickel oxide is present, and copper inclusions into the oxide can be seen, coming from the embedding process of the sample into the resin before cross-sectional characterizations, and meaning that voids were present in the outer layer. Magnesium, aluminum, and iron outward diffusion led to their identification at the top of the oxide, and tungsten is present within the inner layer. Lithium reaction at the surface led to the formation of $LiFeO_2$ as identified with XRD analysis. Finally, at 800°C, an oxide scale can be observed with an increase from

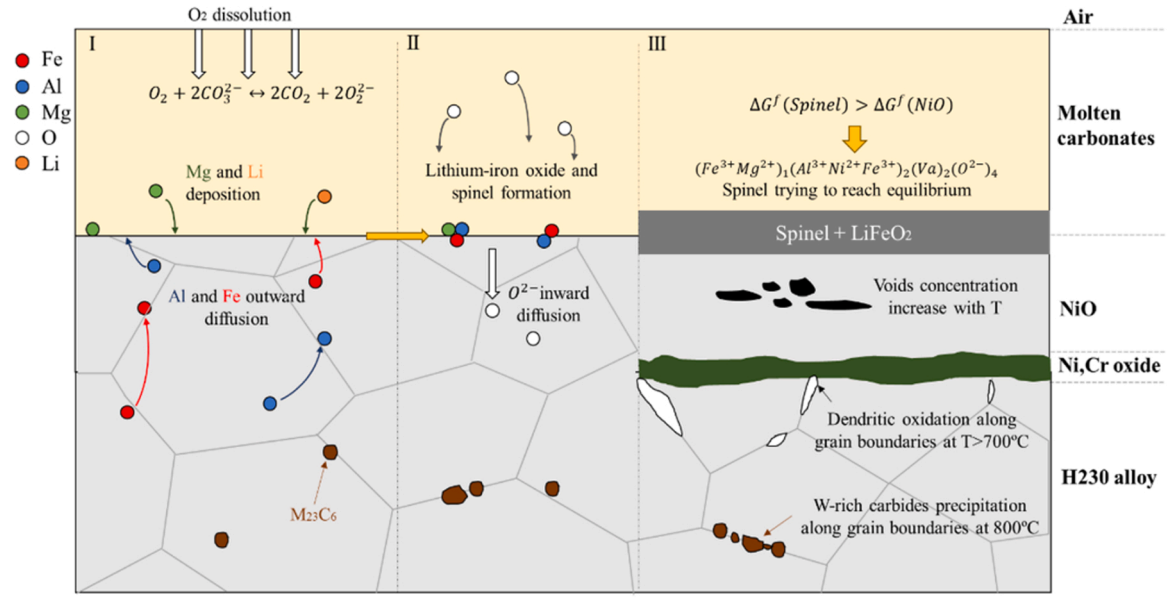

Fig. 21. Scheme of the corrosion mechanism of H230 alloy in molten carbonates.

Table 3
Calculated spinel constituent composition at 700°C, 750°C and 800°C.

Spinel constitution	$(Al^{+3},Fe^{+2},Fe^{+3},Mg^{+2},Ni^{+2})_1$ $(Al^{+3},Fe^{+2},Fe^{+3},Mg^{+2},Ni^{+2},Va)_2$ $(Fe^{+2},Mg^{+2},Va)_2$ $(O^{-2})_4$			
	Temperature (°C)	700	750	800
	Constituent	Site Fraction		
Sublattice 1:				
	Fe^{+3}	0.52536	0.52303	0.5207
	Mg^{+2}	0.41069	0.40234	0.39375
	Al^{+3}	0.06392	0.07457	0.08546
	Ni^{+2}	3E-5	5E-5	9E-5
	Fe^{+2}	3.073E-8	1.043E-7	3.167E-7
Sublattice 2:				
	Al^{+3}	0.46741	0.46169	0.45569
	Ni^{+2}	0.29434	0.29874	0.30341
	Fe^{+3}	0.2372	0.23832	0.23944
	Mg^{+2}	0.00105	0.00125	0.00146
	Fe^{+2}	7.545E-9	2.527E-8	7.594E-8
	Va	1E-12	1E-12	1E-12
Sublattice 3:				
	Va	0.99963	0.99941	0.9991
	Fe^{+2}	3.7E-4	5.9E-4	8.9E-4
	Mg^{+2}	1.071E-7	2.282E-7	4.482E-7
Sublattice 4:				
	O^{-2}	1	1	1

Table 4
Calculated $M_{23}C_6$ constituent composition at 700°C, 750°C and 800°C.

$M_{23}C_6$ constitution	$(Co,Cr,Fe,Mn,Ni)_{20}$ $(Co,Cr,Fe,Mn,Mo,Ni,W)_3$ $(B,C)_6$			
	Temperature [°C]	700	750	800
	Constituent	Site Fraction		
Sublattice 1:				
	Cr	0.97391	0.96941	0.96391
	Ni	0.01843	0.02147	0.02531
	Fe	0.00549	0.00642	0.00745
	Co	0.00204	0.00245	0.00296
	Mn	0.00013	0.00025	0.00037
Sublattice 2:				
	Mo	0.70031	0.58613	0.50188
	W	0.17319	0.25485	0.32338
	Cr	0.12262	0.15325	0.16723
	Ni	0.00315	0.00467	0.00606
	Fe	0.00061	0.0009	0.00115
	Co	0.00005	0.00011	0.0002
	Mn	0.00006	0.00008	0.00011
Sublattice 3:				
	C	1	0.99999	0.99999
	B	2.23E-06	6.02E-06	0.00001

80 μm to 87 μm. Iron high concentration permitted to identify the presence of Ni_2FeO_4 with EDS and $LiFeO_2$ with XRD, along with traces of copper pointed within the corrosion scale, highlighting the unprotective porous structure of these layers that can lead to rapid spallation in case of pore coalescence. Then, nickel oxide can be identified with traces of sodium, chromium, and potassium, and a dendritic growth of the oxide can be observed at grain boundaries.

Thus, the overall corrosion mechanism has been schematically represented on Fig. 21, divided into three steps. In the first step, the oxygen dissolved from the air into the salt is reduced (Eq. 1) while magnesium deposits on the substrate react with outward diffused aluminum, nickel, and iron in the second step, to further oxidize in the third step (Eqs. 2–4), and $LiFeO_2$ formed due to lithium presence, identified at higher temperatures. Long exposures permitted to highlight the further precipitation of spinel phases from NiO precursor, stable at high temperatures. Despite their low concentration, aluminum and iron are present on the top of the corrosion layer. Besides the nickel-chromium oxide spinel structure, the Gibbs free energy of formation of potential phases in a NiO environment with deposition or inward diffusion of magnesium, aluminum and iron was calculated, as seen in Fig. 20, and tends to the preferential reaction formation of a $(Fe^{+3},Mg^{+2})_1$ $(Al^{+3},Fe^{+3},Ni^{+2})_2$ $(Va)_2$ $(O^{-2})_4$ spinel at equilibrium, which composition can be seen on Table 3 for each temperature. Nevertheless, this phase will hardly thrive to reach stability in this environment but can explain the dispersion of elements present in the nickel oxide layer.

$$O_2 + 2CO_3^{2-} \leftrightarrow 2CO_2 + 2O_2^{2-} \quad (3)$$

$$Ni + O_2^{2-} \leftrightarrow NiO + O^{2-} \quad (4)$$

$$2M^{3+} + 3O^{2-} \rightarrow M_2O_3 \quad (5)$$

$$M^{2+} + O^{2-} \rightarrow MO \quad (6)$$

The higher tungsten concentration within the white grains can be identified as a Cr-rich, W carbide $M_{23}C_6$ carbide, as pointed out in past research [20,21]. Moreover, at 800°C, they precipitate linearly at the

grain boundary. Indeed, the evolution of the constituent site fractions of $M_{23}C_6$ were calculated and are gathered on Table 4, and tungsten will tend to diffuse into the carbide at the expense of molybdenum in the second sublattice at higher temperatures. This stable formation lead to the mitigation of tungsten dissolution but may favor the oxide growth at grain boundary.

5. Conclusions

H230 alloy behavior was studied in a molten carbonate environment at 700ºC, 750ºC and 800ºC up to 1000 h in an air atmosphere and thermogravimetric, superficial, and cross-sectional analyses permitted to better understand the corrosion mechanisms of this alloy and the diffusion process of its elements.

The diffusion of nickel and chromium have been identified and led to the formation of a protective bilayer of a nickel oxide above a nickel-chromium oxide at 700ºC, leading to a corrosion rate of 0.019 $\pm$ 0.005 μm/year. At higher temperatures, lithium-iron oxide growth was identified at the material surface by means of XRD analysis and was corroborated by the high presence of iron in outer oxide layers. Indeed, higher diffusion coefficients of aluminum and iron at 750ºC and 800ºC led to the formation of voids and cracks within the oxide scale, enhancing the oxygen and salt inward diffusion, and creating a cascade corrosion mechanism. Moreover, the dendritic dispersion of oxygen inward diffusion along grain boundaries has been pointed out at higher temperatures along with the precipitation of tungsten-rich chromium carbides, that could accelerate this mechanism. Thus, the potential temperature window occurring potentially at the tower receiver of a CSP plant need to be controlled to avoid critical corrosion.

CRediT authorship contribution statement

M. Lambrecht: Conceptualization, Validation, Writing – original draft, Writing – review & editing, Visualization. **M.T. de Miguel:** Conceptualization, Validation, Investigation, Writing – review & editing, Visualization, Project administration. **M.I. Lasanta:** Conceptualization, Methodology, Validation, Investigation, Project administration. **G. García-Martín:** Resources, Writing – review & editing, Project administration. **F.J. Pérez:** Conceptualization, Supervision, Funding acquisition.

Declaration of Competing Interest

The authors declare that they have no known competing financial interests or personal relationships that could have appeared to influence the work reported in this paper.

Data availability

The raw data required to reproduce these findings are available from the corresponding author, Mickaël Lambrecht, upon reasonable request. The processed data required to reproduce these findings are available from the corresponding author, Mickaël Lambrecht, upon reasonable request..

Acknowledgement

This work received funding from the Agencia Estatal de Investigación in the frame of the "Proyectos I + D + I 2020″ program and under project reference number PID2020–115866RB-C22 (PID2020–115866RB-C22/AEI/10.13039/501100011033).

References

[1] D. Ercole, O. Manca, K. Vafai, An investigation of thermal characteristics of eutectic molten salt-based nanofluids, Int. Commun. Heat. Mass Transf. 87 (2017) 98–104.
[2] H. Tian, et al., Enhanced thermal conductivity of ternary carbonate salt phase change material with Mg particles for solar thermal energy storage, Appl. Energy 204 (2017) 525–530.
[3] C.-G. Lee, Analysis of impedance in a molten carbonate fuel cell, J. Electroanal. Chem. 776 (2016) 162–169.
[4] J. Milewski, et al., Supporting ionic conductivity of Li2CO3/K2CO3 molten carbonate electrolyte by using yttria stabilized zirconia matrix, Int. J. Hydrog. Energy 46 (28) (2021) 14977–14987.
[5] N. Navarrete, et al., K2CO3–Li2CO3 molten carbonate mixtures and their nanofluids for thermal energy storage: an overview of the literature, Sol. Energy Mater. Sol. Cells 236 (2022), 111525, https://doi.org/10.1016/j.solmat.2021.111525.
[6] M.Y. Ramandi, P. Berg, I. Dincer, Numerical analysis of transient processes in molten carbonate fuel cells via impedance perturbations, J. Power Sources 231 (2013) 134–145.
[7] H. Sauzet, et al., Redox properties of the carbonate molten salt Li2CO3Na2CO3-K2CO3, Electrochim. Acta 405 (2022), 139765.
[8] P. Tomczyk, M. Mosiałek, Investigation of the oxygen electrode reaction in basic molten carbonates using electrochemical impedance spectroscopy, Electrochim. Acta 46 (19) (2001) 3023–3032.
[9] X. Wei, et al., Thermal conductivity improvement of liquid Nitrate and Carbonate salts doped with MgO particles, Energy Procedia 142 (2017) 407–412.
[10] Y.B. Tao, C.H. Lin, Y.L. He, Preparation and thermal properties characterization of carbonate salt/carbon nanomaterial composite phase change material, Energy Convers. Manag. 97 (2015) 103–110.
[11] Z. Zhang, et al., Enhanced thermal properties of Li2CO3Na2CO3K2CO3 nanofluids with nanoalumina for heat transfer in high-temperature CSP systems, Therm. Anal. Calorim. (2017) 10.
[12] P. Tomczyk, M. Mosiałek, J. Obłąkowski, Investigation of processes occurring at NiO and CoO monocrystalline electrodes in basic molten carbonates using electrochemical impedance spectroscopy, Electrochim. Acta 47 (6) (2001) 945–954.
[13] A.G. Fernández, L.F. Cabeza, Corrosion monitoring and mitigation techniques on advanced thermal energy storage materials for CSP plants, Sol. Energy Mater. Sol. Cells (2019) 9.
[14] A.G. Fernández, et al., Corrosion evaluation of alumina-forming alloys in carbonate molten salt for CSP plants, Renew. Energy 140 (2019) 227–233.
[15] X. Zhuang, W. Liu, X. Xu, Hot corrosion of different alloys in chloride and carbonate molten-salt mixtures under argon atmosphere, Sol. Energy 189 (2019) 254–267.
[16] H.Z. Chen, et al., Corrosion behaviours of iron-chromium-aluminium steel near the melting point of various eutectic salts, Sol. Energy Mater. Sol. Cells 210 (2020), 110510.
[17] H.Z. Chen, et al., Corrosion resistance of iron-chromium-aluminium steel in eutectic molten salts under thermal cycling conditions, Corros. Sci. 173 (2020), 108798.
[18] A. Ibrahim, et al., Molten salts in the light of corrosion mitigation strategies and embedded with nanoparticles to enhance the thermophysical properties for CSP plants, Sol. Energy Mater. Sol. Cells 219 (2021), 110768.
[19] M.T. de Miguel, et al., Temperature effect and alloying elements impact on the corrosion behaviour of the alloys exposed to molten carbonate environments for CSP application, Corros. Sci. 201 (2022), 110274, https://doi.org/10.1016/j.corsci.2022.110274.
[20] H.J. Lee, et al., Microstructure evolution of a Ni–Cr–W superalloy during long-term aging at high temperatures, Mater. Charact. 106 (2015) 283–291.
[21] K. Mo, G.L., H.M. Tung, X. Chen, J.F. Stubbins, High temperature aging and corrosion study on Alloy 617 and Alloy 230, in: Proceedings of the Eighteenth International Conference on Nuclear Engineering ICONE18 Nucle May 17–21, 2010, Xi'an, China ee ing ICONE18 May 17–21, 2010, Xi'an, China.